# Design Concepts for Adaptive Airfoils with Dynamic Transonic Flow Control

M. Trenker*
*Deutsches Zentrum für Luft- und Raumfahrt, German Aerospace Center, D-37073 Göttingen, Germany*

Modifications to design of airfoils for use in unsteady transonic flows are carried out by means of realistic geometry modeling and systematic removal of recompression shocks in the transonic region. A procedure for designing deformable airfoils for helicopter rotor blades is introduced. A baseline shock-free airfoil is created by combining systematic and optimization methods. Two analytical models of deformation are considered. Their ability to control dynamic stall is investigated numerically by using a two-dimensional, time-accurate, implicit Navier–Stokes code. Results indicate the great potential for the controlled deformation of airfoils for helicopter applications. Dynamic stalling of airfoils at high angles of attack and the appearance of strong recompression shocks at low angles of attack and high Mach numbers are reduced significantly. In this way, the results presented will help in extending the design knowledge base for airfoils for helicopter rotors with advanced dynamic stall control.

## Nomenclature

| | | |
|---|---|---|
| $a$ | = | speed of sound |
| $a_n$ | = | coefficients in parametrized-sections (PARSEC) polynomial |
| $c$ | = | chord length |
| $c_d$ | = | aerodynamic drag coefficient |
| $c_l$ | = | aerodynamic lift coefficient |
| $c_m$ | = | aerodynamic moment coefficient |
| $c_p$ | = | pressure coefficient, $(p - p_\infty)/q_\infty$ |
| $f$ | = | frequency |
| $M$ | = | Mach number, $u/a$ |
| $p$ | = | static pressure |
| $q_\infty$ | = | dynamic pressure, $(\rho_\infty u_\infty^2)/2$ |
| $Re$ | = | Reynolds number, $(uc)/\nu$ |
| $T$ | = | scaled dimensionless time, $0 \le T \le 1$ |
| $u, v, w$ | = | local velocities in $x$, $y$, and $z$ directions |
| $X, Y, Z$ | = | Cartesian coordinates referred to $c$ |
| $\alpha$ | = | angle of attack |
| $\nu$ | = | kinematic viscosity |
| $\rho$ | = | density |
| $\omega*$ | = | reduced frequency, $(2\pi f c)/u_\infty$ |

## Introduction

THE idea of adapting the aerodynamic components of flight vehicles to improve aerodynamic performance and control has been the subject of many studies, for example, Refs. 1 and 2. Proposals include systematic shape variations of airfoils and lifting wings. In recent years, practical concepts for deforming airfoils in the transonic speed range for varying operating conditions have gained renewed attention. New materials, refined control mechanisms, and more stringent requirements to reduce fuel consumption have led to several concepts for efficient modification of flow boundaries during flight. Proposed systems make use of elastic, pneumatic, and piezoelectric devices, and there is now a realistic chance that one of these technologies will lead to improvements in commercial aircraft. To achieve this, theoretical and numerical analysts are challenged to refine their tools to model geometrical boundary conditions better including mechanical constraints.[3]

Advanced numerical analysis is also required to model fully viscous effects in compressible flow. The latter is to be developed especially for simulation of unsteady flow phenomena in transonic flow because the periodic performance of helicopter rotor blades, including the occurrence of dynamic stall, may be influenced most favorably by adaptive devices. Because of the superposition of the rotor's rotational speed and the flight speed of the helicopter, the rotor blade section undergoes a variation in its freestream Mach number of approximately $0.3 < M < 0.8$. Nevertheless, transonic flow considerations are necessary because low Mach numbers occur at high angles of attack. This leads, in most cases, to a small supersonic region very close to the leading edge. The recompression shock terminating this supersonic region can be an initiator for dynamic stalling of the airfoil and has, therefore, a strong influence on the flow characteristics.[4]

Improved aerodynamic performance has been obtained by combining large camber modifications of a standard airfoil with local contour flattening based on the transonic design knowledge base.[5] In Ref. 6, an airfoil for a helicopter rotor was deformed by using a sealed slat. The size of the slat was limited to 10% of the chord. The performance of the deforming airfoil was investigated for varying freestream Mach numbers and varying angles of attack. In Ref. 7, dynamic stall control is examined at constant freestream Mach number for a pitching NACA 0012 airfoil with deflection of the leading-edge region of the airfoil. In the study, the effects of different frequencies for the deflection are investigated numerically, as well as the influence of the duration over which the deformation is active. It is known,[4,8,9] that adequate turbulence modeling and appropriate models for transition are of prime importance to predict heavily separated flows adequately at low and transonic Mach numbers. Laminar/transitional leading-edge separation bubbles trigger the dynamic separations in most cases. In Ref. 10, investigations at similar conditions to those presented here were done for different turbulence and transition models.

In this paper, different models for the variation of airfoil geometry are explored. After selecting a proper design point, an initial airfoil is generated. The role of systematic shock-free redesign is investigated by applying the fictitious gas (FG) design method[11] to the initial airfoil. Guided by these results, an optimization method is used to design shock-free airfoils that also show improved aerodynamic characteristics at weak offdesign conditions. These shock-free airfoils are used as baseline airfoils for adapting models for airfoil deformation. The performance of deforming airfoils is analyzed for oscillatory motion together with phase-shifted variations in freestream Mach number. This is done with a view to application in the field of helicopter aerodynamics. The flowfield response to the geometric variations is solved numerically by a two-dimensional,

*Research Position, Institute of Aerodynamics and Flow Technology, Department of High Speed Configurations, Bunsenstr. 10. Member AIAA.

time-accurate, implicit Navier–Stokes code,[12] which was updated by implementing the geometric conservation law (GCL) algorithm[13] to allow also for deforming grids. The code offers the most common turbulence and transition models. The aim of the present study is to define and apply dynamically deforming shapes to control dynamic separation. In this regard, modeling transition in the boundary layer would excessively increase computational time, and there is also a lack of adequate models that could be used. For these reasons, transition is not considered here.

## Choosing a Design Point

Choosing the proper design point for an airfoil undergoing large variations in angle of attack and freestream Mach number can be a difficult task. One obvious choice is to select some kind of average flow condition. This is probably the right choice especially when the airfoil shape is kept unchanged. However, for the present investigation, the design point is chosen to be the highest Mach number/lowest angle of attack combination. The airfoil will be designed using methods for generating shock-free airfoils at the design conditions. To adapt the airfoil to low Mach numbers and high angles of attack, the airfoil will be deformed according to the deformation models described in the section "Models for Airfoil Deformation".

## Initial Airfoil Generation

A combination of a geometric preprocessing tool and a fast flow solver is used to generate an initial airfoil. The airfoil is defined by

$$Z = a_1 X^{\frac{1}{2}} + \sum_{n=2}^{6} a_n X^{n-k} \tag{1}$$

which is a generalized representation of Sobieczky's parametrized-sections (PARSEC) airfoil family.[3] Equation (1) will be applied separately to the airfoil's upper and lower surfaces. Both polynomials are connected by the coefficient $a_1$, which is determined by the leading-edge radius of the airfoil and holds for both polynomials. The coefficients $a_n$ are determined by geometric requirements of the airfoil (location of the maximum thickness, curvature at the maximum thickness, trailing edge information, etc.). The parameter $k$ in Eq. (1) is set to $k = 0.5$.

To calculate the flowfield around the generated airfoil, the flow solver MSES, by Drela and Giles[14] and Drela[15] is used. MSES is an Euler code coupled with a boundary-layer code. The combination of these two tools enables designers to create an initial airfoil based on their aerodynamic knowledge base in an intuitive way. This initial airfoil is shown in Figs. 1 (line a) and 2 (line a) and the corresponding distribution of the pressure coefficient is shown in Fig. 3 (line a). Figure 3 (line a) shows that a recompression shock terminates the supersonic region on the upper side of the airfoil. This leads to the next step in the design process.

## Shock-Free Airfoil Redesign: Manual Relaxation

Systematic shock-free redesign is applied to remove the shock at the design conditions. This is done using the FG-design method combined with an inverse method of characteristics (IMOC)[1] applied to the supersonic region of the flowfield (Fig. 1). The resulting pressure distribution of the shock-free airfoil is shown in Fig. 3 (line b). When the FG-method is used, the real flowfield around the airfoil is computed everywhere except in regions where the local flow velocity exceeds the critical speed. In potential theory for a perfect gas, this supersonic region would be modeled by hyperbolic partial differential equations (PDE). However, the FG method solves an elliptic PDE everywhere in the flowfield. This leads to solutions for the usual, perfect gas in regions where the flow is subsonic and a solution in the formally supersonic region, but for a fictitious subsonic flow. Because recompression shocks are not possible in flows modeled by an elliptic PDE, a shock-free flow (Fig. 1) is achieved. The IMOC is used to determine the flow characteristics for the perfect gas in the region bounded by the sonic line. This requires flow data at the sonic line as initial conditions for marching toward the airfoil to find a new airfoil contour compatible with the smooth sonic line. The new shock-free airfoil is obtained after taking into account
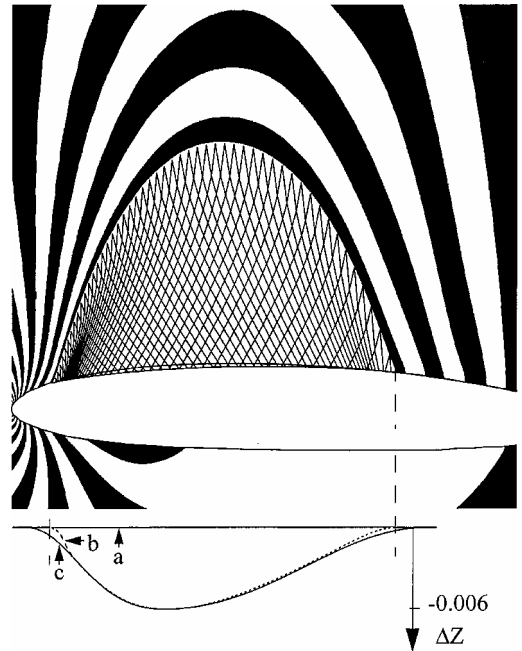


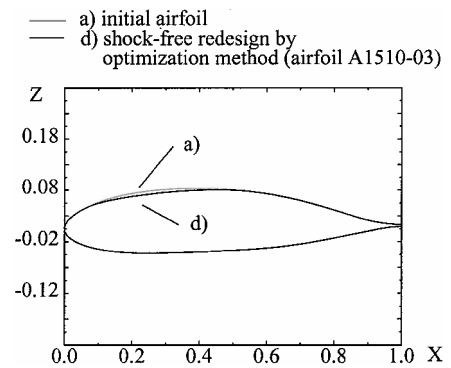**Fig. 1  Isobars and characteristics, subtracting contour difference from the airfoil upper side.**



**Fig. 2  Initial airfoil and final baseline airfoil derived from optimization method.**
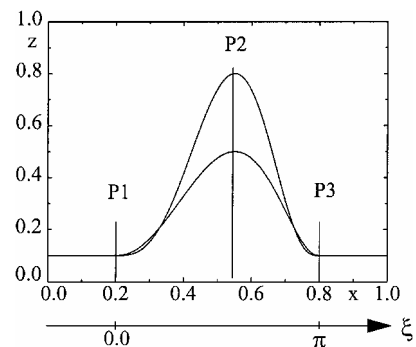


**Fig. 3  Different analytical bump shapes with curvature control at three points.**

some corrections for the boundary-layer thickness. The pressure distribution for the new airfoil is given in Fig. 3 (line b). More thorough descriptions of the FG method and the IMOC may be found in Refs. 16 and 17. Clustering of expansion characteristics, as can be seen in Fig. 1 in the expansion region on the airfoil's upper surface, indicate strong gradients in curvature. In the limit, a series of characteristics merge at one point. This is commonly referred to as the Prandtl–Meyer expansion at a sharp bend. Such singularities, as well
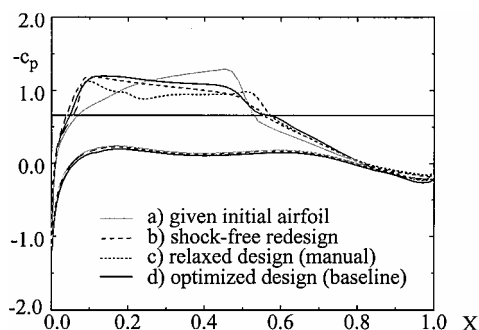
**Fig. 4   Pressure distributions for airfoils during different design steps (MSES results).**



**Fig. 5   Airfoil modification by modeling an SSF.**



**Fig. 6   Airfoil modification by controlling the airfoil's camber line.**



**Fig. 7   Structured grid around airfoil A1510-03.**

as solution ambiguities due to overlapping characteristics, occur if the aerodynamic load (design angle of attack and/or Mach number) is too high. Although well supported by subsonic and fictitious flow analysis, they indicate that no shock-free transonic solution is physically possible. Shock-free design conditions strictly will occur only at design conditions. Therefore, it is practically feasible to modify this design by a relaxation of surface parameters, as shown in Fig. 1. The analytically found surface modification Fig. 1 (line b) will be approximated by a bump function with an extended length Fig. 1 (line c).

This bump function[3] is given by a suitable expression of the form

$$z = z_2 \cdot \sin[\pi f(\xi)]^{g(\xi)} \tag{2}$$

with $z_2$ the maximum height of the bump. Figure 4 shows two different bump shapes. Curvature can be controlled at locations P1, P2, and P3. Local flattening of the airfoil's upper side by subtraction of a bump according to Fig. 1 leads to the airfoil that was used in Ref. 10 as the "baseline rigid airfoil" to adapt the deformation models. In Fig. 1 (line c), the airfoil contour on the upper surface is shown, and Fig. 3 (line c) shows the corresponding pressure distribution.

### Shock-Free Airfoil Redesign by Using Optimization Methods

Because manual relaxation of the shock-free airfoil leads to losses in performance, as can be seen in Fig. 3, it is more efficient to use an optimization method. Therefore, the flow solver[15] is combined with the SIMPLEX optimization method[18] and a geometric preprocessing tool to modify given airfoils. From the FG method, local bump subtraction from the airfoil's upper surface leads to a shock-free or at least to a nearly shock-free airfoil. When the bump function is used [Eq. (2)], various parameters to control the shape of the bump can be specified. The beginning and end of the bump on the airfoil's upper surface are known from the FG method (Fig. 1). Based on experience in choosing bump parameters for this type of application, in most cases, only the maximum bump height $z_2$ and its location need to be determined by the optimization method. Curvature smoothness at start- and endpoints of the bump is ensured.

The resulting airfoil, which was named A1510-03, is shown in Fig. 2 (line d). It serves now as the baseline airfoil for the airfoil deformation models. Its corresponding $c_p$ distribution is shown in Fig. 3 (line d). The aerodynamic coefficients for lift, drag, and moment derived from the MSES code, coupled with the optimization method, are $c_l = 0.576$, $c_d = 0.009$, and $c_m = -0.0425$.

### Models for Airfoil Deformation

An exact definition of flow boundary conditions by mathematically explicit functions has proven most beneficial for the quality of numerical simulations. This is especially true if the goal of the analysis is to find shape modifications for improved aerodynamics. In the present case, two possibilities for an airfoil deformation are investigated.

Rotation of rigid airfoil front and/or rear parts around given hinge points and their elastic connections, as shown in Fig. 5, is one way
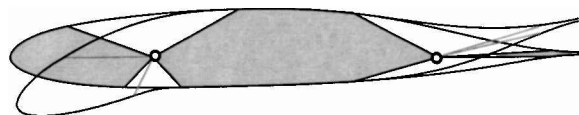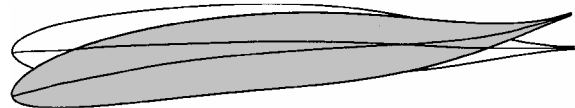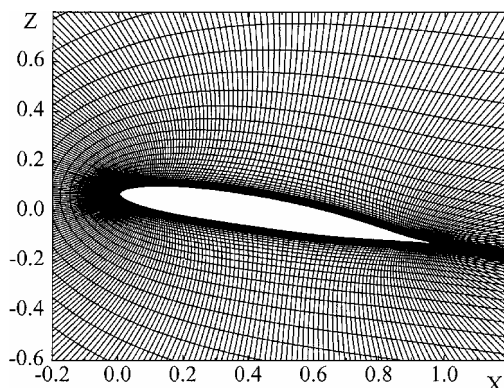
to define a deforming airfoil. Such a model of sealed slats and/or flaps (SSF model) with smooth curvature connections may be realized mechanically. Being in a position to actually choose all of the necessary parameters rather freely to optimize unsteady flow quality gives the designer the chance to not only fulfill conditions that may be set by (current) industrial relevance, but also to take these as a starting point for finding new specifications for new parameters and defining their range regardless of the present status of mechanical realization. This was the motivation for finding an alternative way to define some effective parameters for creating airfoil deformation specification. As is well known from classical aerodynamic theory, airfoils can be defined as being composed by a camber line and a superimposed thickness distribution. Accordingly, an airfoil deformation model can be defined by shaping the camber line and keeping the thickness distribution unchanged [Fig. 6, smooth camber variation model (SCV) model]. What is needed in this case is information about the camber line of the initial airfoil to be deformed. The SCV model employs a smoother function for the camber line than does the resulting local camber line shape of the SSF model in the hinge point area if slat and flap are rotated. A cubic function should, in most practical cases, be suitable for modeling the airfoil's initial camber line.

### Grid Generation

An elliptic grid generation method[19] was used to generate the grid around the airfoil (Fig. 7). The rigid-body motion and the deformation is performed in such a way that the outer flowfield boundary is fixed in space. A $385 \times 81$ grid was found suitable. The smallest grid element height is $2 \times 10^{-6}$ times the chord of the airfoil.

### Flow Solver

The flow solver used for simulating the viscous flow around the pitching and deforming airfoil is based on the method by Beam and Warming.[20] Its capabilities to predict dynamic stall on airfoils was validated using the well-accepted AGARD test cases.[21] Detailed information about the implementation and the accuracy of this code may be found in Refs. 12 and 22. The code was used in previous

work, for example, Refs. 5, 6, 10, 12, and 22. It was updated with the GCL algorithm,[13] to allow deforming grids. The grid is calculated for each time step by a linear interpolation from a set of predefined grids that include the deformation, as well as the pitching motion of the airfoil. Because of an implemented vortex correction at the outer boundary, it was found sufficient to set the far field 11 chord lengths away from the airfoil.[12] The turbulence model by Spalart and Allmaras[23] is used throughout the following calculations. Transition from laminar to turbulent flow in the boundary layers was neglected, for reasons mentioned in the Introduction; thus, the whole boundary layer was assumed to be turbulent.

## Rigid-Body Motion

The reduced frequency of the airfoil motion, $\omega_*$, was set to 0.1. For a Reynolds number of $8 \times 10^6$ at design Mach number of 0.73, this results in an oscillatory frequency $f$ of about 7 Hz. The sinusoidal variation of the angle of attack and Mach number are shown in Fig. 8. The design point is defined at $T = 0.75$. Here $\alpha$ reaches its minimum value of 2.2 deg, corresponding to the highest Mach number of 0.73.

First, the flowfield of the baseline rigid airfoil is investigated under pitching and superimposed lead/lag motion of the airfoil, as shown in Fig. 8. To illustrate the flow quality, plots of $c_p$ vs $X$ are shown for different times in the cycle in Fig. 9. The airfoil starts at the mean angle of attack of 12.2 deg and a freestream Mach number of 0.5 at time $T = 0$. There are some high suction peaks because of strong acceleration starting from the stagnation point. Strong separation on the airfoil's suction surface occurs at $T = 0.25$ as the airfoil moves toward the highest angle of attack and, correspondingly, the lowest Mach number. The shedding of the dynamic stall vortex can be seen as waves are transported toward the trailing edge and, subsequently, into the wake of the airfoil. The airfoil moves on its downstroke toward its lowest angle of attack at $T = 0.75$, and the flow reattaches
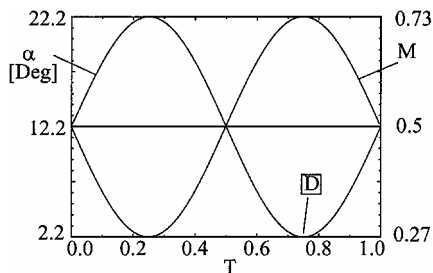


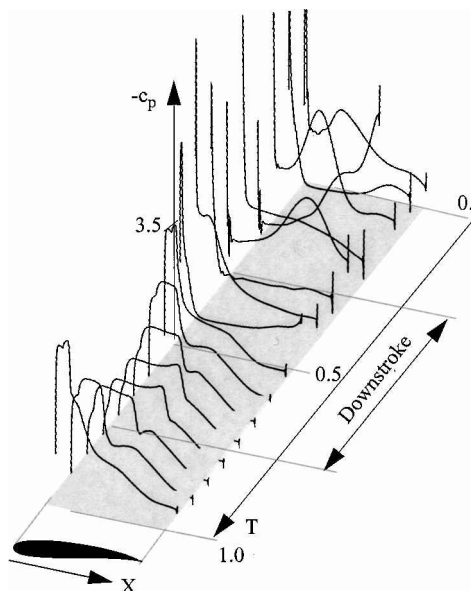Fig. 8 Relation between angle of attack and Mach number.



Fig. 9 Pressure coefficient for the baseline rigid-airfoil suction side.

approximately at $T = 0.5$. At the design point, $T = 0.75$, the distribution of the pressure coefficient shows only a weak shock and only slight differences from the distribution in Fig. 3 (line d), indicating that the steady initial design still seems well suited for this reduced frequency. From similar investigations,[6,10] for this type of application, at least in the region of $T \approx 0.75$, a quasi-steady flow can be assumed at low reduced frequencies, that is, $\omega_* = 0.1$ in this case. At $T > 0.75$, the angle of attack is increased, and the freestream Mach number decreases. This leads to an upward movement of the compression shock toward the leading edge. The solution at $T = 1.0$ coincides with the one at $T = 0.0$ due to the periodicity of the boundary conditions for angle of attack and freestream Mach number.

The solution of a steady calculation at $\alpha = 12.2$ deg and $M = 0.5$ serves as a starting point for the unsteady calculations. The unsteady calculation is taken to be converged when the solutions for the aerodynamic coefficients over multiple periods coincide. The discretization in time was 200,000 time steps per period, which results in a Courant–Friedrichs–Lewy number of 270. This value lies within the range for which stable solutions have been obtained for similar investigations.[8] One period takes approximately 2.6-h CPU time on the DLR, German Aerospace Center, supercomputer NEC SX5. It usually takes up to three periods for a converged solution to be reached.

## Airfoil Deformation

Airfoil deformation is done using the SSF and the SCV models according to Figs. 5 and 6 with large elastic connections and reduced rigid portions of the contour for the SSF model. Figure 10 shows all necessary parameters and their values. The starting and ending points of the elastic parts of the airfoil are given in terms of a percentage of the chord length of the nondeformed airfoil. Locations of hinge points are given by their $(x, z)$ coordinates. To compare the effectiveness of different deformation models, the same amount of deformation for both models was ensured, as shown in Fig. 11. The values for the deflection of leading- and trailing-edge parts differ because for the SSF model they refer to the baseline rigid airfoil but for the SCV model they refer to the slope of the camber line of the baseline rigid airfoil. The airfoil deformation is in phase with the variation of $\alpha$. This means that the airfoil will be deflected to the maximum values at the highest angle of attack, as shown in Figs. 10 and 11. At the design point, no deformation results in the baseline airfoil. To deform the airfoil, only the deflection of leading- and trailing-edge parts for the SSF model is varied. For the SCV model the slopes of the camber line at leading and trailing edge are varied during the deformation.
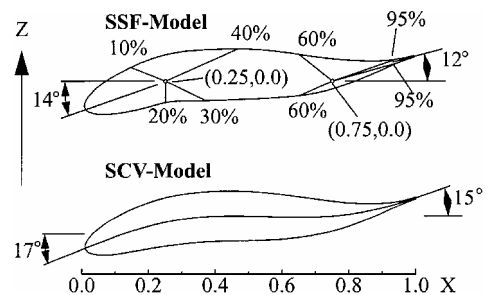


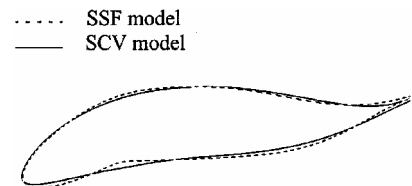Fig. 10 Maximum deflection values of the deformation models.



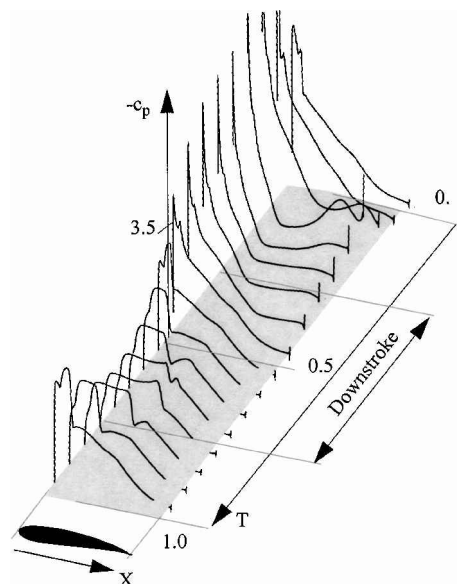Fig. 11 Deformed airfoils at maximum deformation (scaled).

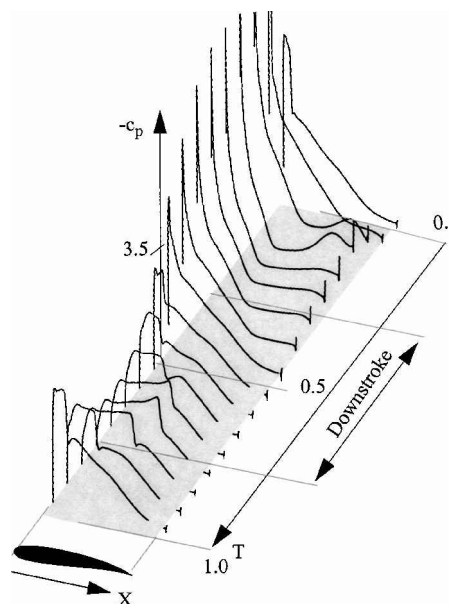**Fig. 12   Pressure coefficient for the deforming SSF airfoil's suction side.**



**Fig. 13   Pressure coefficient for the deforming SCV airfoil's suction side.**

### SSF Model

Deforming the baseline airfoil according to the SSF model shows improvements of the flow quality over most of the airfoil's upper surface. Note that the pressure distribution in Fig. 12 has a much smoother appearance compared to the rigid airfoil. In the region $0 < T < 0.5$, the shedding of the dynamic stall vortex is nearly suppressed. A small vortex can be detected, and its appearance and strength is governed by the degree of deformation. When a higher degree of deformation is allowed, the tendencies toward separation can be minimized. However, it was observed that stronger deformation resulted also in some decrease in lift. Therefore a tradeoff has to be found between allowable vortex shedding and lift produced. At the design point, $T = 0.75$, the pressure distribution is similar to that for the rigid airfoil. Because of deformation of the airfoil at $T > 0.75$ the shock moving toward the leading edge is weaker than for the rigid-airfoil case.

### SCV Model

When the SCV model is used for deforming the airfoil, the resulting pressure distribution in Fig. 13 appears globally similar to
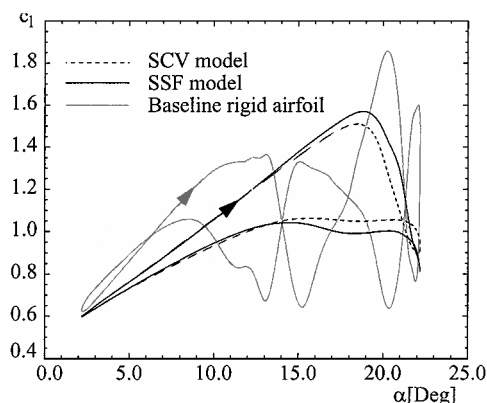


**Fig. 14   Lift coefficient vs $\alpha$ for rigid airfoil, SSF, and SCV models.**
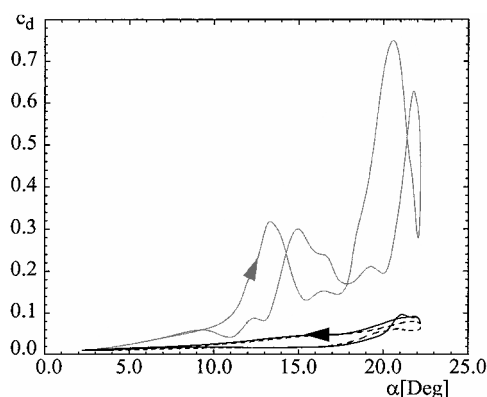


**Fig. 15   Drag coefficient vs $\alpha$ for rigid airfoil, SSF, and SCV models.**

the results of the SSF model. In the region $0 < T < 0.5$, a rather weak dynamic stall vortex is shed from the airfoil's upper surface and spills into the wake. For $T > 0.5$, the recompression shock appears to be weaker for the SCV model than in the case of the SSF model. At $T \approx 0.6$, the SCV model results in a smoother pressure distribution behind the shock.

The overall performance of the airfoil deformation models can be assessed by plotting the aerodynamic coefficients $c_l$, $c_d$, and $c_m$ vs $\alpha$. Both geometric models deliver clean curves for $c_l$, $c_d$, and $c_m$ coefficients, with a maximum in $c_l$ at an angle of attack of about 19 deg. This is about three times higher than the static value at the design condition. Vortex shedding leads to a loss in $c_l$ near the maximum $\alpha$. This results in the hysteresis loop, seen in Fig. 14. The SSF model produces a slightly higher $c_l$ than the SCV model during the downstroke. The small loops at the highest angle of attack, indicating dynamic vortex shedding, coincide with the corresponding pressure distributions in Figs. 12 and 13. The drag coefficient is highest at maximum $\alpha$, with a maximum value of less than 0.1 (Fig. 15). This is about eight times smaller than for the rigid airfoil. The moment coefficient (Fig. 16) is nearly constant over the whole period with a change in sign near the maximum $\alpha$ for the SCV model. In the region $0.5 < T < 1.0$, both deformation models result in very similar values for the aerodynamic coefficients.

For helicopter applications, there is a demand for balanced lift for the main rotor over the whole period $0 < T < 1$. $M^2 c_l$ is proportional to the lift force produced and is, therefore, plotted vs the dimensionless time for three different airfoils in Fig. 17. The solid lines correspond to the rigid baseline airfoil A1510-03 and the dynamically deformed airfoil according to Fig. 10 using the SSF model. The dashed line corresponds to the rigid baseline airfoil, which is statically deformed with the SSF model. The angles for leading and trailing edge deflection are half the values shown in Fig. 10. The size and position of the elastic parts are kept unchanged. The airfoil is deformed initially and then kept rigid over the whole period $0 < T < 1$. As
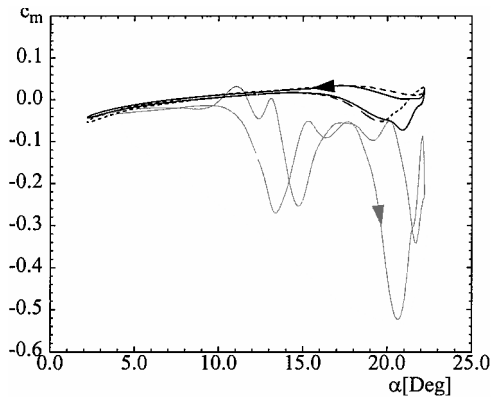
**Fig. 16   Moment coefficient vs $\alpha$ or rigid airfoil, SSF, and SCV models.**
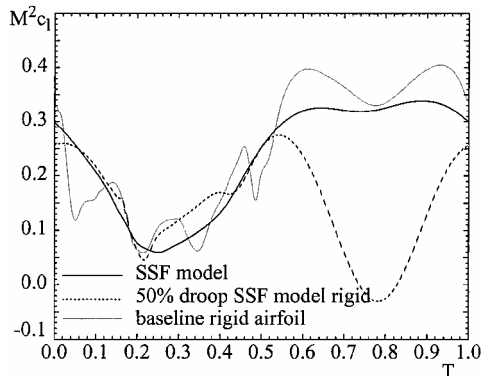


**Fig. 17   Lift proportional factor $M^2 c_l$ vs the dimensionless time $T$.**

expected, the baseline rigid airfoil shows some large separated regions in the period $0.0 < T < 0.5$. This is indicated by the oscillations in Fig. 17. In the transonic speed region, $0.5 < T < 1.0$, some lift overshoot is obtained. The SSF model shows the same global behavior as the rigid baseline airfoil, but without the oscillations. To achieve a globally balanced lift over the whole period, various parameters can be changed. The range of the angle-of-attack variation, together with all of the parameters in the deformation model can be used to balance the lift. One could reduce the design value of $c_l$, which is in this case 0.576. This would lead to a decrease of $M^2 c_l$ in the transonic region $0.5 < T < 1.0$. Increasing $\alpha$ in the region of $0.0 < T < 0.5$ and adjusting the deformation model parameter would lead to the desired globally balanced lift distribution. At $T \approx 0.75$, both the rigid baseline airfoil and the SSF model are similar in shape and, therefore, produce nearly the same amount of lift. The airfoil that is kept rigid with 50% degree of deformation has some similarities to airfoils currently used in helicopters. With the SSF model and some fixed, moderate degree of deformation, such airfoils can be generated on the basis of some suitable baseline airfoil.

## Conclusions

Dynamic flow control by adaptive, dynamically deforming airfoils is presented as a rational design procedure for the baseline airfoil and accurate analytical definition of deformation models. The effectiveness of deforming airfoils is tested under unsteady conditions for angles of attack and freestream Mach numbers typical of helicopter applications. If, from a mechanical point of view, the use of dynamically deformed components is realistic for this type of application, the presented studies suggest the following design process.

When the design point of the initial rigid airfoil is chosen to be at the highest Mach number and lowest angle of attack, the demands on performance in the transonic speed regime can be fulfilled. An optimization method is used to find the bump shape, which, when

subtracted from the airfoil's upper side, produces a shock-free baseline airfoil. However, when it comes to the high-angle-of-attack dynamic stall region, airfoil deformation models, such as the ones presented, give an ability to control the flow and achieve a balanced lift distribution over the whole period.

Models with two different geometrical variations were tested numerically for their effectiveness for dynamic flow control. Both models show great promise in defining flow boundaries. It was found that using quintic functions for modeling deformations with SSF gives good results, especially during the upstroke, where the drooped nose dramatically reduces flow expansion and recompression shock strength. From a practical point of view, the SSF model may find application to adaptive helicopter rotor blades. Modeling airfoil deformation by the SCV model still needs a more careful approach to find optimum parameters for the camber line variation. Low-speed applications for the SCV model and suitable three-dimensional geometry extensions can be found by modeling animal motions, for example, flapping bird wings and fish bodies. Also the SCV approach may be useful for controlling an airplane by changing the whole wing in a variable twist manner rather than by use of ailerons.

Some uncertainties arise from numerical transition and turbulence modeling. As pointed out by many authors, taking care of the laminar boundary layer plays an important role in predicting dynamic stall. The lack of appropriate models still gives only limited possibilities for exact prediction.

## References

[1]Sobieczky, H., and Seebass, A. R., "Adaptive Airfoils and Wings for Shock-Free Supercritical Flight," Invention Disclosure, Rept. EES TFD 78-02, Univ. of Arizona, Tucson, AZ, 1978.

[2]Sobieczky, H., "Gasdynamic Knowledge Base for High Speed Flow Modelling," *New Design Concepts for High Speed Air Transport*, edited by H. Sobieczky, International Centre of Mechanical Science Courses and Lectures, Vol. 366, Springer, Vienna, 1997, pp. 105–120.

[3]Sobieczky, H., "Parametric Airfoils and Wings," *Notes on Numerical Fluid Mechanics*, edited by K. Fuji and G. S. Dulikravich, Vol. 68, Vieweg, Wiesbaden, Germany, 1998, pp. 71–88.

[4]Fung, K.-Y., and Carr, L., "An Analytical Study of Compressibility Effects on Dynamic Stall," Frank Seiler Research Lab., Rept. FJSRL-TR 88-0004, U.S. Air Force Academy, Colorado, Sept. 1988.

[5]Geissler, W., and Sobieczky, H., "Unsteady Flow Control on Rotor Airfoils," AIAA Paper 95-1890, July 1995.

[6]Geissler, W., Trenker, M., and Sobieczky, H., "Active Dynamic Flow Control Studies on Rotor Blades," Research and Technology Organisation Advanced Vehicle Technology Panel Symposium: Active Control Technology for Enhanced Performance Operation Capabilities of Military Aircraft, Land Vehicles and Sea Vehicles, May 2000.

[7]Reuster, J. G., and Baeder, J. D., "A Computational Investigation of Dynamic Stall Alleviation Using Leading Edge Deformation," AIAA Paper 4121, Aug. 2000.

[8]Ekaterinaris, J. A., and Platzer, M. F., "Numerical Investigation of Stall Flutter," *Journal of Turbomachinery*, Vol. 118, April 1996, pp. 197–203.

[9]Ekaterinaris, J. A., and Platzer, M. F., "Computational Prediction of Airfoil Dynamic Stall," *Progress in Aerospace Science*, Vol. 33, No. 11–12, April 1998, pp. 759–846.

[10]Trenker, M., Geißler, W., and Sobieczky, H., "Airfoils with Dynamic Transonic Flow Control," AIAA Paper 2000-4419, Aug. 2000.

[11]Sobieczky, H., "Verfahren für die Entwurfsaerodynamik moderner Transportflugzeuge," DLR, German Aerospace Center, Rept. FB-85-43, Göttingen, Germany, Dec. 1985.

[12]Geissler, W., "Instationäres Navier-Stokes-Verfahren für beschleunigt bewegte Profile mit Ablösung," German Aerospace Center, Rept. DLR-FB 92-03, Göttingen, Germany, Jan. 1992.

[13]Thomas, P. D., and Lombard, C. K., "Geometric Conservation Law and its Application to Flow Computations on Moving Grids," *AIAA Journal*, Vol. 17, No. 10, 1979, pp. 1030–1037.

[14]Drela, M., and Giles, M. B., "ISES: A Two-Dimensional Viscous Aerodynamic Design and Analysis Code," AIAA Paper 87-0424, Jan. 1987.

[15]Drela, M., "A User's Guide to MSES V2.1," Massachusetts Inst. of Technology, Computational Fluid Dynamics Lab., Cambridge, MA, June 1992.

[16]Sobieczky, H., "Analytical Tools for Systematic Transonic Design," *International Journal of Numerical Methods in Engineering*, Vol. 22, No. 2, 1986, pp. 309–326.

[17]Li, P., and Sobieczky, H., "Computation of Fictitious Gas Flow with Euler Equations," *Acta Mechanica*, Supplement, Vol. 4, 1994, pp. 251–257.

[18]Nelder, J. A., and Mead, R., "A Simplex Method for Function Minimization," *Computer Journal*, Vol. 7, No. 4, 1965, pp. 308–313.

[19]Sorensen, R. L., "A Computer Program to Generate Two-Dimensional Grids About Airfoils and Other Shapes by the Use of Poisson's Equation," NASA TM-81198, May 1980.

[20]Beam, R. M., and Warming, R. F., "An Implicit Factored Scheme for the Compressible Navier–Stokes Equations," *AIAA Journal*, Vol. 16, No. 4, 1978, pp. 393–402.

[21]Landon, R. H., "Compendium of Unsteady Aerodynamic Measurements," AGARD Rept. 702, Aug. 1983.

[22]Trenker, M., Über den Entwurf und die Anwendung adaptiver Geometrien zur instationären Strömungsbeeinflussung," German Aerospace Center, Rept. DLR-FB 2001-25, Göttingen, Germany, Nov. 2001.

[23]Spalart, P. R., and Allmaras, W. R., "A One-Equation Turbulence Model for Aerodynamic Flows," *La Recherche Aerospatiale*, Vol. 1, No. 5, 1994, pp. 24–37.